Optical absorption study of iron-substituted zirconia and yttria-stabilized zirconia using experimental measurements and many-body perturbation theory

Shunshun Liu [1,*] Victor K. Champagne, III [2,†] David R. Clarke [2,‡] and Prasanna V. Balachandran [1,3,§]

[1]*Department of Materials Science and Engineering, University of Virginia, Charlottesville, Virginia 22904, USA*

[2]*Harvard John A. Paulson School of Engineering and Applied Sciences, Harvard University, Cambridge, Massachusetts 02134, USA*

[3]*Department of Mechanical and Aerospace Engineering, University of Virginia, Charlottesville, Virginia 22904, USA*

(Received 9 May 2024; accepted 31 July 2024; published 29 August 2024)

Yttria-stabilized zirconia (YSZ) coatings have been developed for high temperature energy applications including gas turbines. The objective of this work is to understand how aliovalent Fe substitution affects the optical absorption spectrum of the host YSZ and ZrO_2 systems in the ultraviolet–visible–near infrared wavelength range (from 245 to 2500 nm) using both experimental and computational techniques. In the Fe-substituted ZrO_2 system, phase-pure (>99% purity) samples were synthesized in the monoclinic crystal structure, whereas Fe substitution in YSZ resulted in a two-phase mixture of coexisting tetragonal and monoclinic phases. Optical property characterization performed at room temperature revealed two broad absorption bands in both systems: one centered around 1000 nm and the other centered around 500 nm. Tauc plot analysis of the optical absorption data showed that as the Fe concentration increases, the optical band gaps of both materials systems decrease. Many-body perturbation theory methods, based on G_0W_0 and the Bethe-Salpeter equation, were used to computationally model the optical absorption spectrum as a function of Fe substitution in the tetragonal and monoclinic crystal structures of YSZ and ZrO_2. Supercells were constructed and several Fe- and/or Y-atom configurations were explored in Zr sites. Charge compensating O vacancies were introduced to maintain electrical neutrality. The computations reveal that the observed optical excitations centered around 1000 nm likely have an excitonic character due to defect states, whose origin is traced to the electronic transitions between Fe-3*d* and Fe-3*d* orbitals. Intriguingly, both the tetragonal and monoclinic crystal structures appear to support local polyhedral distortions that promote excitations in the 1000 nm wavelength region. The excitation centered around 500 nm is attributed to the optical band gap of these materials. The outcomes of this work shed light on the radiative properties of Fe-substituted YSZ with implications in thermal barrier coating composition design.

DOI: 10.1103/PhysRevMaterials.8.085203

I. INTRODUCTION

Yttria-stablized zirconia (YSZ) in its tetragonal prime form has been of considerable interest as a thermal barrier coating (TBC) material on account of its exceptionally low thermal conductivity at high temperatures and high fracture toughness [1–5]. For the majority of TBC applications in gas turbine engines, its low phonon or thermal conductivity has been sufficient to provide thermal protection to the underlying metal alloy components. However, with increasing gas temperatures at the entrance to the hot-section turbine, the importance of thermal radiative transport through the coatings as a parallel heat transfer path to thermal conduction is being reexamined. [6–9]. This is especially important since TBCs, despite containing extensive porosity that scatters thermal radiation, has a very low absorption in the visible and near infrared (IR) because of its large band gap (E_g). The radiative (q_{rad}) contribution to the total heat transfer through the TBC layer is determined by the optical properties such as absorption, emission, scattering, and refractive index [10]. Recent works of Clarke and co-workers have shown that the optical properties of the TBC materials can play a significant role in impacting the q_{rad} term and temperature distribution through the coating [9,11]. One of the solutions to minimizing the radiative heat transfer and the bond-coat temperature involve designing TBCs with tailored refraction and absorption indices, yet retaining their low thermal conductivity.

The optical E_g in cubic zirconia stabilized with different concentrations of yttria has been well documented for single crystals [12,13]. Buchanan and Pope performed optical measurements on cubic YSZ and doped YSZ (rare-earth and transition metal elements) and observed a translucent behavior in the 0.35–7 μm wavelength range [14]. However, the optical measurements on single crystal YSZ by Park and Blumenthal revealed an E_g of 3.26 eV at room temperature (although the authors did not discuss the crystal structure of their YSZ single crystal) [15]; it is most likely they were cubic as no other single crystals existed at that time. In the same work [15], Park and Blumenthal showed that E_g decreases linearly with temperature (T), which was captured by the linear expression, $E_g(T) = 3.4\text{–}5.16 \times 10^{-4}T$, where T is temperature in kelvin (K). At 1800 K, the E_g is then projected to reduce to 2.47 eV. A recent experimental work on 8YSZ thin films (3–4 mol % Y_2O_3-stabilized ZrO_2 in the tetragonal-prime phase) reported

*Contact author: ejf5wk@virginia.edu
†Contact author: vchampagne@g.harvard.edu
‡Contact author: clarke@seas.harvard.edu
§Contact author: pvb5e@virginia.edu

a E_g of 5.8 eV at room temperature using the electron energy loss spectroscopy [16]. The temperature-dependent optical reflectivity of fully dense, polycrystalline tetragonal YSZ up to 1673 K over a frequency range of 400–1500 cm^{-1} (6.67–25 μm) has been reported [17]. The authors observed little change in the refractive index (n) and absorption coefficient (α) above 833 cm^{-1} (<12 μm), whereas below 833 cm^{-1} these values changed significantly with temperature. Eldridge *et al.* measured the optical absorption coefficients for plasma-sprayed YSZ coatings up to 1633 K, and showed a definite temperature dependence of the absorption edge with a shift to shorter wavelengths at higher temperatures [18].

Although there are many published computational studies on the properties of the electronic, elastic, phononic, and thermodynamic properties of doped ZrO_2 systems [19,20] using the Kohn-Sham density functional theory (DFT), few studies have calculated the optical properties (e.g., optical absorption spectra) for this materials class using many-body perturbation theory (MBPT) methods, such as the *GW*–Bethe-Salpeter equation (BSE) [21–24]. Avdoshenko and Strachan calculated the optical responses of defect-free and oxygen-deficient tetragonal ZrO_2 using Kohn-Sham DFT calculations at 0 K [25]. The authors predicted a large high-temperature emissivity in oxygen-deficient ZrO_2. More recently, Götsch *et al.* also used the Kohn-Sham DFT to calculate the optical properties of tetragonal YSZ (6 mol % YSZ) at 0 K [16]. The authors used a $2 \times 2 \times 2$ supercell structure to model the crystal structure and electronic structure. Unfortunately, a lack of high-fidelity optical absorption data from beyond-DFT methods, such as the MBPT, affects the reliable interpretation of the experimental data.

In this paper, we report a combined experimental and first-principles calculation (DFT + *GW*-BSE) approach to develop an understanding of the optical absorption spectrum of Fe-substituted YSZ (Fe-YSZ) and Fe-substituted ZrO_2 (Fe-ZrO_2) systems. The effect of adding Fe_2O_3 as a sintering aid during processing of YSZ and ZrO_2 is well documented in the literature [26–29]. In addition, Fe^{3+} is also explored as a cubic phase stabilizer [30–32] and coloring agent in dental implants [33–35]. Published x-ray diffraction (XRD), Raman spectroscopy, and Mössbauer spectroscopy studies have argued that Fe occupies both substitutional and interstitial sites in the lattice [29,36,37] and a detailed x-ray absorption study has also provided insights into plausible local atomic configurations of the Fe^{3+} as a substitutional defect in the lattice [38]. Magnetic susceptibility and Mössbauer spectroscopy studies have also revealed that Fe is in its high-spin 3+ paramagnetic state [30,36,39].

The objective of our work is to investigate the relationship between local bond distortions and optical absorption in the ultraviolet-visible-near infrared (UV-Vis-NIR) wavelength range (from 245 to 2500 nm) of the host YSZ and ZrO_2 using both experimental and computational techniques. Our experimental measurements shed light on the relationship between Fe solubility in YSZ and ZrO_2, phase purity, optical E_g, and room temperature optical absorption spectrum. Several Fe-YSZ and Fe-ZrO_2 configurations (with oxygen vacancies, $\ddot{V}_O$, to maintain charge neutrality) are simulated in both tetragonal and monoclinic crystal structures. The *GW*-BSE calculated optical absorption spectra predict visible light and near-IR absorption, and the spatial electron/hole distribution suggest that there is also an excitonic effect localized at Fe-3d orbitals. The outcome of this work has implications in providing insights to explore transition metal based cation substitution design strategies for influencing heat transfer by absorption of thermal radiation, as well as ways of altering the color of these oxides.

II. METHODS

A. Materials synthesis

The Fe-ZrO_2 and Fe-YSZ samples were synthesized using a modified-Pechini method which involves complexing cations in an aqueous-organic solution [40]. The process involves dissolving metal nitrate or chloride salts in de-ionized water with a chelating agent, ethylenediaminetetraacetic acid [Sigma-Aldrich, BioUltra, anhydrous, ⩾99% (titration)] to form metal cation complexes. The precursors were metal salts: zirconium dichloride oxide hydrate (Strem Chemicals, 99.9%), yttrium nitrate hexahydrate (Sigma-Aldrich, 99.8%), and iron (III) nitrate nonahydrate (Sigma-Aldrich, 98 + %). The solution was poured into an alumina crucible and the remaining water was evaporated and then calcined, leaving only the metal oxide powder. A complete account of the precise experimental details of this synthesis method can be found in Ref. [41]. The powder particles produced by this method are typically <100 nm. To produce disk-shaped pellets for characterization, the powder was first pressed in a hardened steel die at a pressure of 200 MPa for 3 min, then sintered at 1500 °C for 4 h. For the optical and thermal characterization, samples 1 mm thick were prepared.

B. Materials characterization

XRD patterns of the materials were taken using a Panalytical X'Pert Pro in the Bragg-Brentano geometry using a Cu $K\alpha$ source. The Rietveld refinements of the XRD patterns were done using the HIGHSCORE PLUS software from Malvern Panalytical.

Diffuse reflectance measurements were made using a Hitachi U-4100 spectrophotometer in the UV-Vis-NIR range (245–2500 nm) with a barium sulfate–coated integrating sphere accessory. A baseline was taken using a Spectralon diffuse reflectance standard and the resulting reflectance spectrum was corrected with the calibration from Labsphere. The doped zirconia disks were taken to be optically thick meaning that the sum of the reflectance and absorbance is equal to unity.

Using the Kubelka-Munk theory and Tauc plots, the E_g as a function of Fe-doping concentration was calculated. The Kubelka-Munk function, $F(R_\infty)$, is equal to

$$F(R_\infty) = \frac{(1 - R_\infty)^2}{2R_\infty} = \frac{K}{S}, \tag{1}$$

where R_∞ is the diffuse reflectance for an infinitely thick material, K is the optical absorption coefficient, and S is the optical scattering coefficient. Making the assumption that the E_g is a direct allowed transition, the Kubelka-Munk function (i.e., the absorption) can be related to the E_g by

$$[h\nu F(R_\infty)]^2 = A(h\nu - E_g), \tag{2}$$

where h is Planck's constant, ν is the frequency and A is a proportionality constant. The quantity $[h\nu F(R_\infty)]^2$ was plotted against $h\nu$, and the x intercept from the equation of the line drawn using the x-y coordinates of the inflection point with the slope at the inflection point was taken to be the E_g.

C. Density functional theory and many-body perturbation theory

Spin-polarized first-principles calculations were performed based on the Kohn-Sham DFT as implemented in the open-source plane-wave pseudopotential code, QUANTUM ESPRESSO (QE) [42,43]. We chose the generalized gradient approximation (GGA), Perdew-Burke-Ernzerhof exchange–correlation functional, and the SG15 optimized norm-conserving Vanderbilt pseudopotentials for all calculations [44,45]. The kinetic energy cutoff was set to 60 Ry for the wavefunctions, and the Brillouin zone was sampled using a Γ-centered Monkhorst-Pack k mesh for all calculations [46]. The optimized tetragonal YSZ supercell ($2 \times 2 \times 2$) lattice parameters were taken from the published work of Götsch *et al.* [16]. This supercell consisted of 14 Zr atoms, 2 Y atoms, and 31 O atoms (47 atoms in total). Since Zr and Y are nominally in their 4+ and 3+ charge states, respectively, one O vacancy was introduced to maintain charge neutrality. We then relaxed the internal atomic coordinates until the total force was less than 10^{-4} Ry/bohr. In the case of monoclinic structures, the initial unit cell lattice parameters were taken from the work of Smith and Newkirk [47]. We first optimized the unit cell using the variable-cell geometry optimization procedure in QE and then built a $2 \times 1 \times 2$ supercell. Similar to the tetragonal structure, the monoclinic supercell consisted of 14 Zr atoms, 2 Y atoms and 31 O atoms, whose internal atomic coordinates were relaxed until the total force convergence was achieved ($\leqslant 10^{-4}$ Ry/bohr). In addition to YSZ, we also consider Fe-substituted YSZ and ZrO_2. In the case of Fe-YSZ, one of the Y atoms was substituted by the Fe atom. We then relaxed the internal atomic coordinates. In the case of Fe-ZrO_2, both the Y atoms were replaced by the Fe atoms. We assumed Fe to have a nominally 3+ charge state based on the published Mössbauer spectroscopy data [36,39]. We explored three independent Fe-YSZ and Fe-ZrO_2 configurations. In each case, we changed the local Y-Fe or Fe-Fe nearest neighbor distance. In total, we considered two compositions: Fe-YSZ and Fe-ZrO_2. For each composition, we considered two crystal structures: tetragonal and monoclinic. Finally, for each crystal structure, we simulated three independent local atomic configurations. Self-consistent field (SCF) calculations were carried out, followed by non-SCF calculations (using a uniform k mesh of $4 \times 4 \times 4$) to set up the YAMBO database. All relaxed atomic configurations, along with other data, are given in the Supplemental Material that accompanies this paper [48].

Since the mean-field DFT-GGA approximation is known to underestimate the fundamental E_g, we used the MBPT within the G_0W_0 approximation as implemented in the YAMBO code (version 5.1) to obtain the quasiparticle (QP) correction [49,50]. In the YAMBO code, the plasmon-pole approximation for the inverse dielectric function was applied. The screening matrix size (response block size) was set to 5 Ry. A total number of 500 bands with 311 unoccupied bands were used for the polarization, and several other parameters were also tested for convergence (see Fig. S1 in the Supplemental Material). To accelerate the convergence, the closure relation technique developed by Bruneval and Gonze was applied in the G_0W_0 calculation [51]. The Bethe-Salpeter kernel was set up with 12 valence bands and 8 conduction bands, and the kernel was solved by diagonalizing the Hamiltonian. Optical absorption spectra were calculated by solving the BSE with the G_0W_0 QP energy correction, where the electric field was applied along the [111] direction of the supercells. The optical absorption spectra were generated with a Lorentzian broadening of 0.1 eV. The dielectric function, absorption spectrum, and the G_0W_0-BSE simulated Tauc plot of each structure were provided in the Supplemental Material, where the Tauc plot was calculated with the assumption of direct transition from the computed absorption coefficient. Finally, we estimate the binding energies of the excitonic excitations by subtracting the G_0W_0 band gap ($E_g^{G_0W_0}$) from exciton energy (E_λ) using the equation given below [52]:

$$E_b = E_g^{G_0W_0} - E_\lambda. \tag{3}$$

The optical properties spectra are calculated from the G_0W_0-BSE and independent particle approximation (IPA) computed dielectric functions using

$$n^2 = \tfrac{1}{2}\left(\sqrt{\epsilon_1^2 + \epsilon_2^2} + \epsilon_1\right), \tag{4}$$

$$k^2 = \tfrac{1}{2}\left(\sqrt{\epsilon_1^2 + \epsilon_2^2} - \epsilon_1\right), \tag{5}$$

$$\alpha = \frac{4\pi k}{\lambda}, \tag{6}$$

where n is the refractive index, k is the extinction coefficient, α is the absorption coefficient, and the wavelength λ is converted from photon energy by $\lambda = 1240/E$ nm. The computed real part (ϵ_1) and the imaginary part (ϵ_2) of the dielectric function can be found in Figs. S2–S5 with both G_0W_0-BSE and G_0W_0-IPA output. The n and k are also computed and the data is given in the Supplemental Material (Figs. S6 and S7). The G_0W_0-BSE and G_0W_0-IPA absorption spectra are overlaid in Figs. S8 and S9 to show the contribution of the excitonic effect. The G_0W_0-BSE calculated Tauc plots are given in Figs. S10 and S11. As noted above, we only included 20 bands in the BSE calculation. As a result, we interpret the optical properties [e.g., n, k, and $\alpha(\lambda)$] at only a qualitative level. We also tested the impact of different Lorentzian broadening values on the G_0W_0-BSE calculated optical absorption spectra using the GALORE package [53]. The outcomes are discussed in Figs. S12 and S4(F).

III. RESULTS AND DISCUSSION

A. Experimental results

1. Phase identification by XRD

The phase compositions of the 1, 2, 3, and 6 mol % Fe-ZrO_2 (see Fig. 1) and Fe-YSZ (see Fig. 2) samples were determined using the Rietveld refinement of the XRD data. The goodness of fit (GOF) and weighted profile R-factor (R_{wp}) values from the Rietveld analysis are also given in Table I .

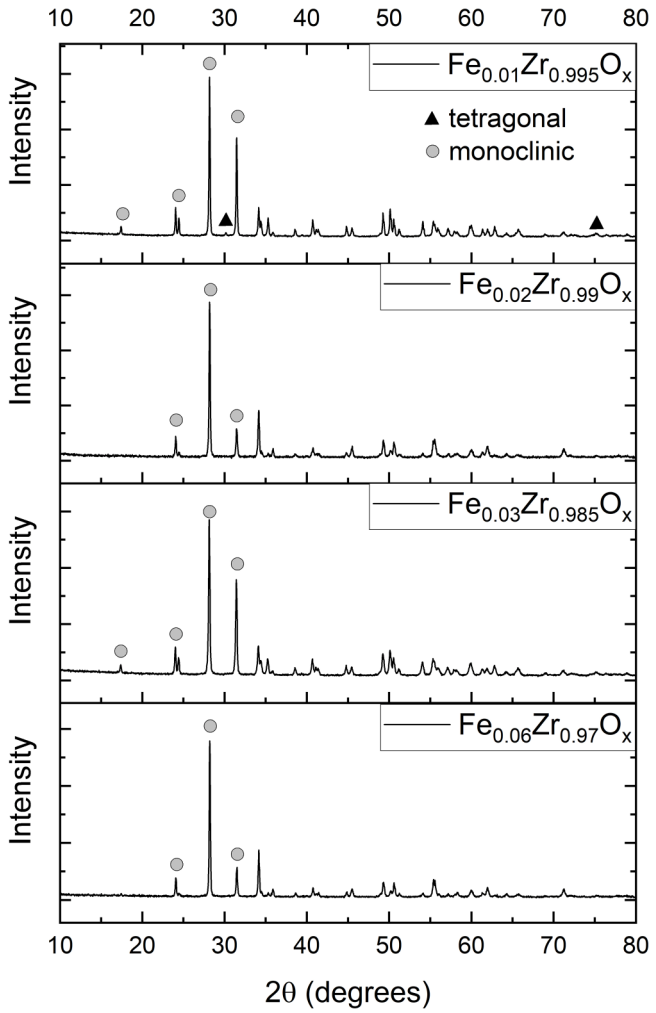

FIG. 1. XRD patterns with labeled phases for four different concentrations of Fe concentration in ZrO_2. Each of the samples was >99% monoclinic.

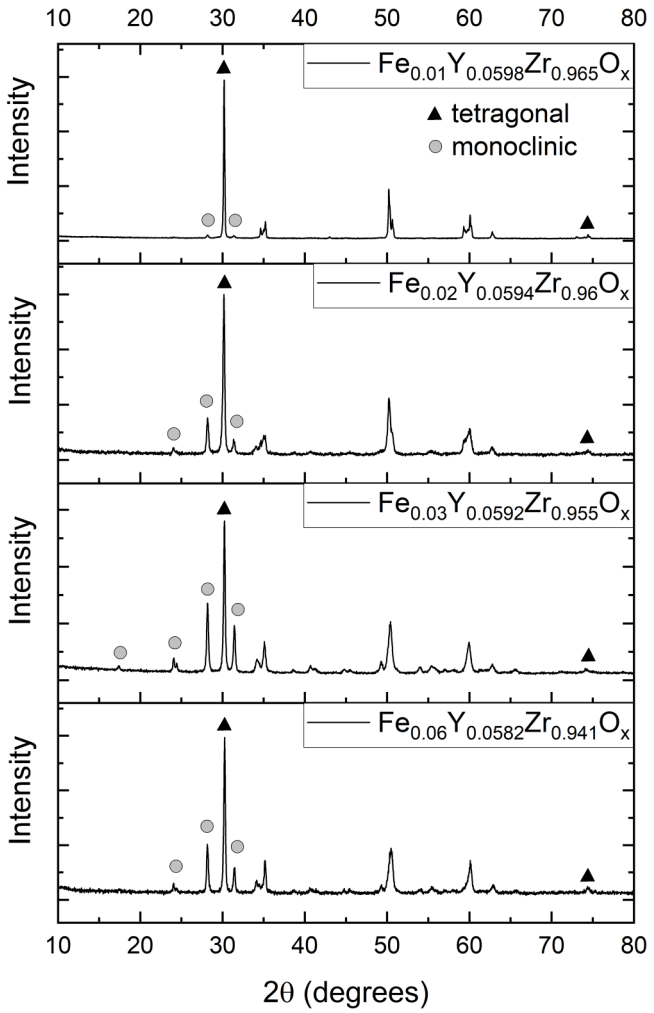

FIG. 2. XRD patterns with labeled phases for four different concentrations of Fe concentration in YSZ. The monoclinic content increases with Fe content.

The Fe-ZrO_2 samples were all >99% monoclinic phase, consistent with previous research on the ZrO_2-FeO pseudobinary phase diagram [54] where the tetragonal phase is not expected to exist at temperatures below 1172 °C. The Fe-YSZ samples showed a general trend of decreasing the tetragonal phase and increasing the monoclinic phase from 83% tetragonal in the 1 mol % Fe-YSZ composition to 60% tetragonal in the 6 mol % Fe-YSZ composition. Although the Fe-doped samples appeared brown in color similar to iron oxide, neither the Fe-ZrO_2 nor the Fe-YSZ XRD spectra showed any evidence of other oxide phases including iron oxide phases indicating that the iron was taken into solid solution. The full phase quantification results from the Rietveld refinement are shown in Table I.

2. Optical absorption and band gap estimates

The Fe-ZrO_2 and Fe-YSZ materials showed broad absorption peaks in the UV-Vis-NIR range, characteristic of transition metals. There were two identifiable broad absorption bands: one centered around 1000 nm and the other centered around 500 nm. As shown in Figs. 3 and 4, the hemispherical spectral absorption increased with increasing Fe concentration throughout the range of the measurement from 245 to 2500 nm as the baseline absorption also increased

TABLE I. Phase quantification results for Fe-ZrO_2 and Fe-YSZ from the Rietveld refinement. Goodness of fit (GOF) and weighted profile *R*-factor (R_{wp}) values from the Rietveld analysis performed using the HIGHSCORE PLUS software from Malvern Panalytical are included for each sample. Since we only measured one XRD pattern per sample, we do not have statistics for multiple measurements for phase quantification.

Sample	% tetragonal	% monoclinic	GOF	R_{wp}
$Fe_{0.01}Zr_{0.995}O_x$	0.8	99.2	1.40	8.45
$Fe_{0.02}Zr_{0.99}O_x$	0	100	2.49	27.18
$Fe_{0.03}Zr_{0.985}O_x$	0.2	99.8	1.29	7.38
$Fe_{0.06}Zr_{0.97}O_x$	0	100	2.68	27.42
$Fe_{0.01}Y_{0.0598}Zr_{0.965}O_x$	83.4	16.6	1.32	13.79
$Fe_{0.02}Y_{0.0594}Zr_{0.96}O_x$	71.5	28.5	1.26	13.33
$Fe_{0.03}Y_{0.0592}Zr_{0.955}O_x$	48.1	51.9	1.31	7.67
$Fe_{0.06}Y_{0.0582}Zr_{0.941}O_x$	59.6	40.4	1.13	12.04

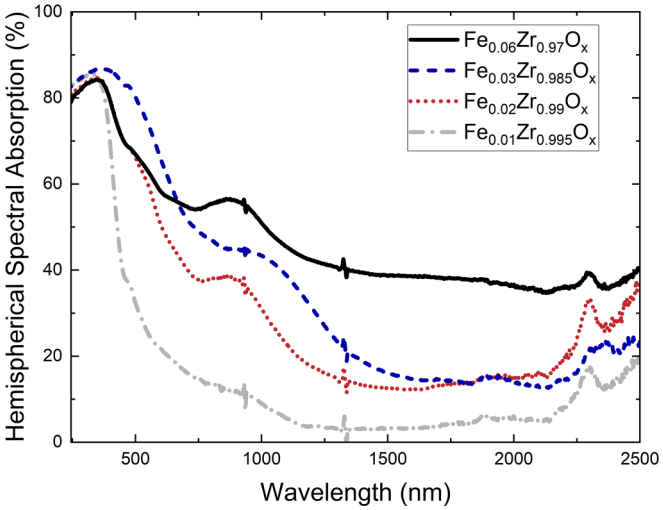

FIG. 3. Hemispherical spectral absorption for four different concentrations of Fe substitution in ZrO_2.

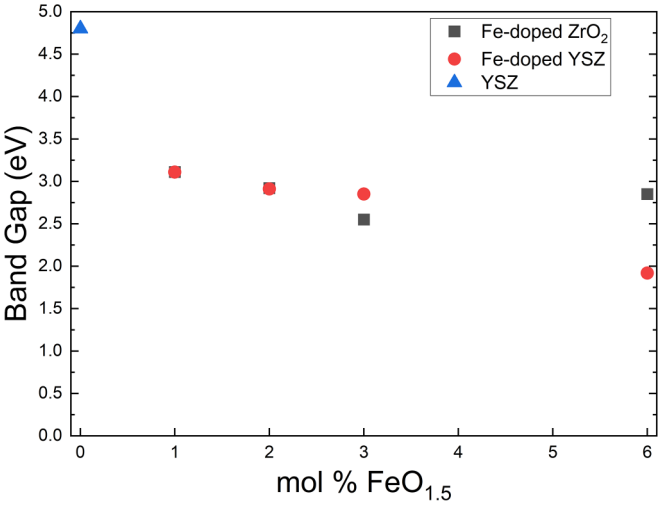

FIG. 5. Calculated band gaps from experimentally measured absorption and Tauc plots as a function of Fe concentration.

with Fe doping. The estimated E_gs as a function of Fe doping derived from the Tauc plots are shown in Fig. 5. The E_g for YSZ was 4.80 eV, which agrees well with the literature data [32]. Generally, as the concentration of Fe increased, the E_g decreased in both the ZrO_2 and YSZ materials.

B. DFT crystal structures

In Fig. 6, we show the DFT relaxed atomic configurations for both Fe-YSZ and Fe-ZrO_2 compositions in the tetragonal crystal structure. The Y-O and Fe-O polyhedra are highlighted to aid the visualization and interpretation of the results. Six independent defect configurations were studied, three each for T-Fe-YSZ [Figs. 6(a)–6(c)] and T-Fe-ZrO_2 [Figs. 6(d)–6(f)]. The location of O vacancy ($\ddot{V}_O$) in the structure is given in the Fig. 6 caption. In Table II, the extracted bond distortions data from the relaxed structures are given. There are two sets of bond distortions data for T-Fe-ZrO_2 (Fe1 vs Fe2) because we have two independent FeO_x polyhedra in this composition. In the case of T-Fe-YSZ, the configuration C shown in Fig. 6(c) had the lowest total energy, where the Fe and Y atoms share common O atoms and are separated by 3.59 Å. The other two atomic configurations (A and B) are at least 20 meV/atom higher in energy. However, in the case of T-Fe-ZrO_2, configuration E [shown in Fig. 6(e)] had the lowest total energy where the distance between the two Fe atoms is 5.26 Å. Intriguingly, the configurations D and F shown in Figs. 6(d) and 6(f), respectively, are only 11.83 and 5.6 meV/atom higher in total energy compared to that of Fig. 6(e).

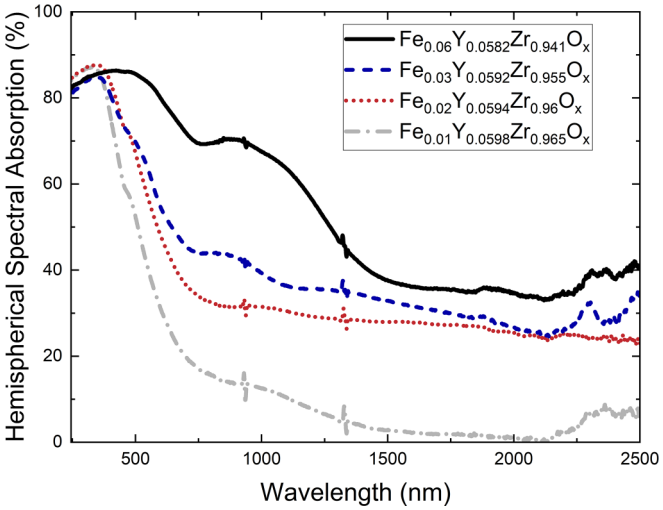

FIG. 4. Hemispherical spectral absorption for four different concentrations of Fe substitution in YSZ.

In terms of FeO_x bond distortions, although the effective coordination number of Fig. 6(a) is similar to that of Fig. 6(b), the FeO_x polyhedron in Fig. 6(a) has a relatively smaller volume of 6.076 $Å^3$. We attribute this to the smaller average Fe-O bond length in this polyhedron. In the T-Fe-ZrO_2 structures, the Fe2-O polyhedra corresponding to the configurations E and F have smaller polyhedral volume compared to that of the D configuration. We attribute this to the relatively smaller Fe2-O bond length and smaller FeO_x effective coordination number.

In Fig. 7, we show the DFT relaxed atomic configurations in the monoclinic crystal structures. Similar to the tetragonal structures, six independent defect configurations were studied for the monoclinic structures: three each for M-Fe-YSZ [Figs. 7(a)–7(c)] and M-Fe-ZrO_2 [Figs. 7(d)–7(f)]. Bond distortions data extracted from the relaxed structures are given in Table III. The lowest energy configuration for M-Fe-YSZ and M-Fe-ZrO_2 is Figs. 7(a) and 7(d), respectively, where the Y-Fe and Fe-Fe atoms are furthest from each other. Our calculated ΔE data also indicates that all three configurations are within 11.6 meV/atom in both M-Fe-YSZ and M-Fe-ZrO_2 compositions. In terms of the FeO_x polyhedron, both M-Fe-YSZ and M-Fe-ZrO_2 exhibit similar bond distortions (see Table III). This is unlike the tetragonal structures, where we find a large variance in the FeO_x bond distortions.

In summarizing the effects of iron substitution, the FeO_x polyhedron in both the tetragonal and the monoclinic crystal structures exhibit distinct local bond distortions. The

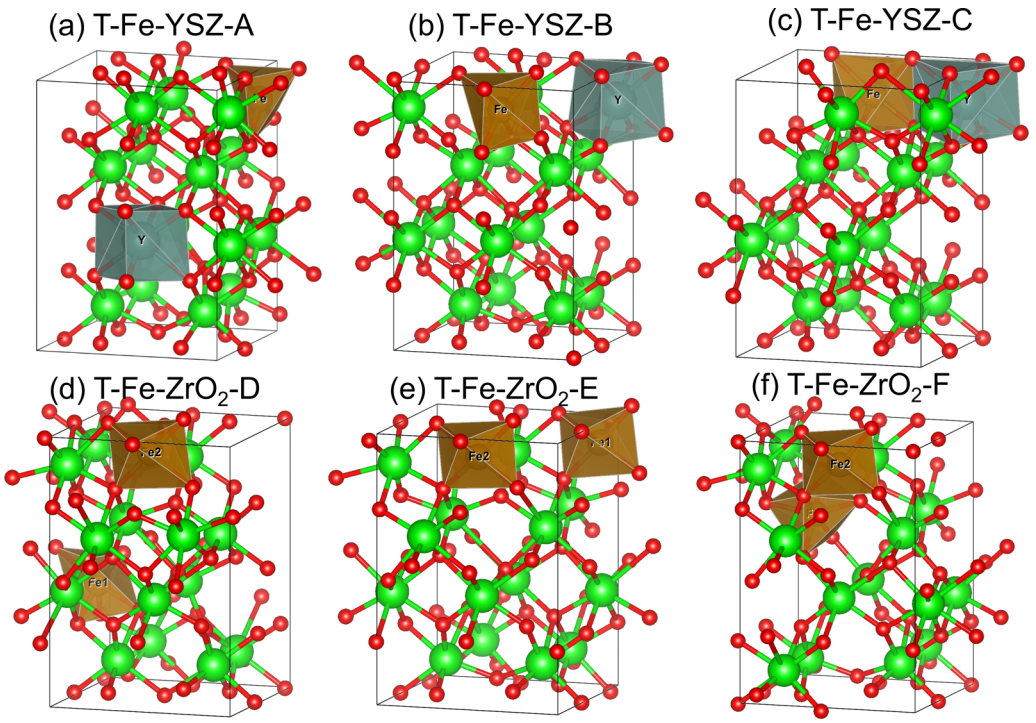

FIG. 6. DFT relaxed six tetragonal crystal structures are shown in two rows. The three structures shown in (a)–(c) correspond to T-Fe-YSZ with three different Fe-Y bond distances. Similarly, the three structures shown in (d)–(f) represent T-Fe-ZrO_2 with three different Fe-Fe bond distances. The Zr and O atoms are shown as green and red spheres, respectively. The Fe-centered polyhedron with the maximum Fe-O bond length of 2.447 Å is shown in brown. The Y-centered polyhedron with the maximum Y-O bond length of 2.625 Å is shown in beige green. In (a) T-Fe-YSZ-A, the $\ddot{V}_O$ is located between YO_x and ZrO_x polyhedra that we denote as Y-$\ddot{V}_O$-Zr. In (b) T-Fe-YSZ-B, the $\ddot{V}_O$ is at Zr-$\ddot{V}_O$-Zr. In (c) T-Fe-YSZ-C, the location of $\ddot{V}_O$ is Fe-$\ddot{V}_O$-Zr. In (d) T-Fe-ZrO_2-D, the $\ddot{V}_O$ is at Zr-$\ddot{V}_O$-Zr, In (e) T-Fe-ZrO_2-E, the $\ddot{V}_O$ is at Zr-$\ddot{V}_O$-Zr, and in (f) T-Fe-ZrO_2-F, the $\ddot{V}_O$ is at Zr-$\ddot{V}_O$-Zr. All six crystal structures have the same lattice parameters (see Table II).

Fe-O bonds are undercoordinated in the tetragonal structures when compared to that of the monoclinic structures. In both structures, the effective Fe-O coordination number is lower than that of the Zr-O coordination number, which agrees well with the x-ray absorption spectra based local structure analysis from Li *et al.* [38]. In the Fe-ZrO_2 system, the local neighborhood has three possible configurations: Zr-O-Zr, Fe-O-Fe, and Zr-O-Fe. However, in the Fe-YSZ system, in addition to Zr-O-Zr, Fe-O-Fe, and Zr-O-Fe, it is also reasonable to expect three additional local neighborhoods: Zr-O-Y,

TABLE II. DFT calculated total energy difference (ΔE), bond lengths, and bond distortions in the tetragonal Fe-YSZ and Fe-ZrO_2 supercells. In the Fe-ZrO_2 simulation cell, we have two independent Fe atoms that we denote as Fe1 and Fe2 in the table below. We used DFT to relax the internal coordinates of each configuration, while the lattice parameters are kept constant at: $a = b = 7.19$ Å, $c = 10.35$ Å, $\alpha = 90^\circ$, $\beta = 90^\circ$, and $\gamma = 90^\circ$. The Tauc plots for the optical band gap can be found in Fig. S10, and their fundamental band gaps (DFT and G_0W_0 QP corrected) are shown in Table S2 in the Supplemental Material. Atomic magnetic moments from DFT for the Fe atoms are given in Table S4 in the Supplemental Material.

	T-Fe-YSZ			T-Fe-ZrO_2		
Tetragonal supercell	A	B	C	D	E	F
d(Y-Fe) or d(Fe-Fe) (Å)	7.09	5.17	3.59	7.74	5.26	3.45
ΔE (meV/atom)	28.94	23.15	0	11.83	0	5.60
Average Fe-O bond length in the Fe-O polyhedron (Å)	1.952	2.049	2.033	Fe1: 2.035 Fe2: 2.038	1.991 1.957	2.011 1.973
FeO_x polyhedral volume (Å^3)	6.076	10.165	10.075	Fe1: 10.206 Fe2: 10.420	9.694 4.981	10.233 5.048
FeO_x distortion index	0.022	0.063	0.058	Fe1: 0.033 Fe2: 0.036	0.031 0.032	0.026 0.029
FeO_x effective coordination number	4.887	4.925	5.058	Fe1: 5.714 Fe2: 5.448	5.670 4.742	5.775 4.813

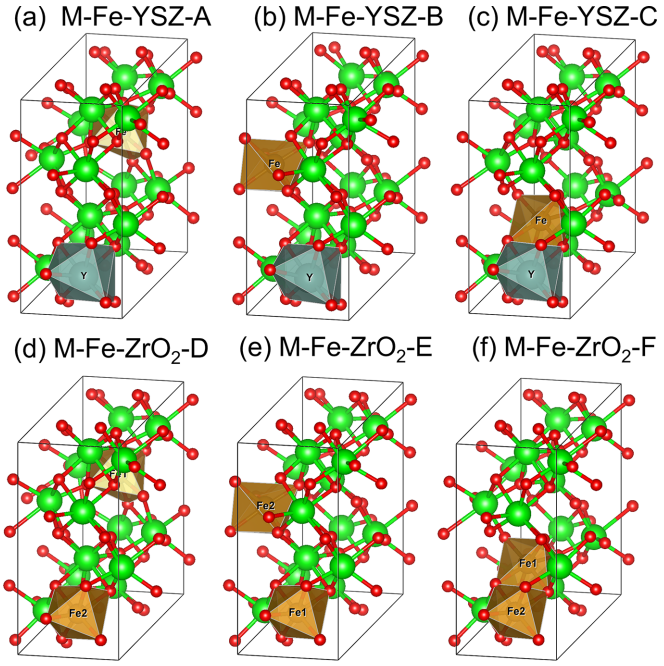

FIG. 7. DFT relaxed crystal structures of three monoclinic Fe-YSZ (a)–(c) and three monoclinic Fe-ZrO_2 (d)–(f) atomic configurations. The Zr and O atoms are shown in green and red spheres, respectively. The Fe-centered polyhedron with the maximum Fe-O bond length of 2.447 Å is shown in brown, and the Y-centered polyhedron with the maximum Y-O bond length of 2.625 Å is shown in beige green. In (a) M-Fe-YSZ-A, the oxygen vacancy ($\ddot{V}_O$) is located between ZrO_x and ZrO_x polyhedra that we denote as Zr-$\ddot{V}_O$-Zr. In (b) M-Fe-YSZ-B, the $\ddot{V}_O$ is at Zr-$\ddot{V}_O\ddot{V}_O$-Zr. In (c) M-Fe-YSZ-C, the location of $\ddot{V}_O$ is Zr-V_O-Zr. In (d) T-Fe-ZrO_2-D, the $\ddot{V}_O$ is at Zr-$\ddot{V}_O$-Zr, In (e) M-Fe-ZrO_2-E, the $\ddot{V}_O$ is at Zr-$\ddot{V}$-Zr, and in (f) M-Fe-ZrO_2-F, the $\ddot{V}_O$ is at Zr-$\ddot{V}_O$-Zr. All six crystal structures use the same lattice parameters (see Table III).

Fe-O-Y, and Y-O-Y. This subtle, but important, difference affects how we interpret the optical properties of Fe-YSZ and Fe-ZrO_2 systems. From the measured XRD data (Fig. 1), we confirmed that the Fe-ZrO_2 samples are made of a >99% phase-pure monoclinic structure. Therefore, we have used the three crystal structures shown in Figs. 7(d)–7(f) to calculate the optical absorption spectrum, which in turn will be used to compare and interpret the measured optical absorption spectrum (Fig. 3). On the other hand, the interpretation of the measured optical absorption spectrum (Fig. 4) is relatively complex because the measured XRD data (Fig. 2) suggests that the samples have both tetragonal and monoclinic crystal structures in the microstructure. We conjecture that our interpretation of the G_0W_0-BSE calculated optical absorption spectrum for Fe-YSZ must take into account all six local neighborhoods (Zr-O-Y, Fe-O-Y, Y-O-Y, Zr-O-Zr, Fe-O-Fe, and Zr-O-Fe) to explain the experimentally measured data (Fig. 4).

C. G_0W_0-BSE optical absorption spectra and excitonic analysis

The G_0W_0-BSE calculated optical absorption spectra for all 12 computed crystal structures are shown in Fig. 8. In addition, we also overlaid the G_0W_0-BSE calculated optical absorption spectrum of T-YSZ in each subfigure, which has no optical absorption for wavelengths >500 nm. The large optical E_g of 5.09 eV for T-YSZ predicted by G_0W_0-BSE agrees closely with the experimentally measured E_g of 4.8 eV for YSZ (blue triangle in Fig. 5). Experimental data (measured at room temperature) suggests that the broad absorption band centered around 500 nm (∼2.48 eV) corresponds to the onset of the optical E_g (bottom of the conduction band). The other broad absorption band centered around 1000 nm is suggested to arise from the midgap states due to the presence of the defects. In the G_0W_0-BSE calculated optical absorption spectra,

TABLE III. DFT calculated total energy difference (ΔE), bond lengths, and bond distortions in the monoclinic Fe-YSZ and Fe-ZrO_2 supercells. In the Fe-ZrO_2 simulation cell, we have two independent Fe atoms that we denote as Fe1 and Fe2 in the table below. We used DFT to relax the internal coordinates of each configuration, while the lattice parameters are kept constant at $a = 10.28$ Å, $b = 5.24$ Å, $c = 10.61$ Å, $\alpha = 90°$, $\beta = 99.519°$, and $\gamma = 90°$. The Tauc plot for the optical band gap can be found in Fig. S11, and their fundamental band gap (DFT and G_0W_0 QP corrected) can be found in Table S3 in the Supplemental Material. Atomic magnetic moments from DFT for the Fe atoms are given in Table S4 in the Supplemental Material.

	M-Fe-YSZ			M-Fe-ZrO_2		
Monoclinic supercell	A	B	C	D	E	F
d(Y-Fe) or d(Fe-Fe) (Å)	8.10	6.22	3.35	8.01	5.99	3.19
ΔE (meV/atom)	0	11.57	5.79	0	2.89	11.57
Average Fe-O bond length in the Fe-O polyhedron (Å)	1.994	2.020	2.006	Fe1: 1.996 Fe2: 2.033	2.027 2.024	2.008 2.031
FeO_x polyhedral volume (Å^3)	10.047	10.417	10.342	Fe1: 10.132 Fe2: 10.704	10.587 10.440	10.419 10.733
FeO_x distortion index	0.036	0.042	0.037	Fe1: 0.036 Fe2: 0.034	0.032 0.044	0.036 0.030
FeO_x effective coordination number	5.518	5.391	5.507	Fe1: 5.489 Fe2: 5.492	5.634 5.359	5.534 5.663

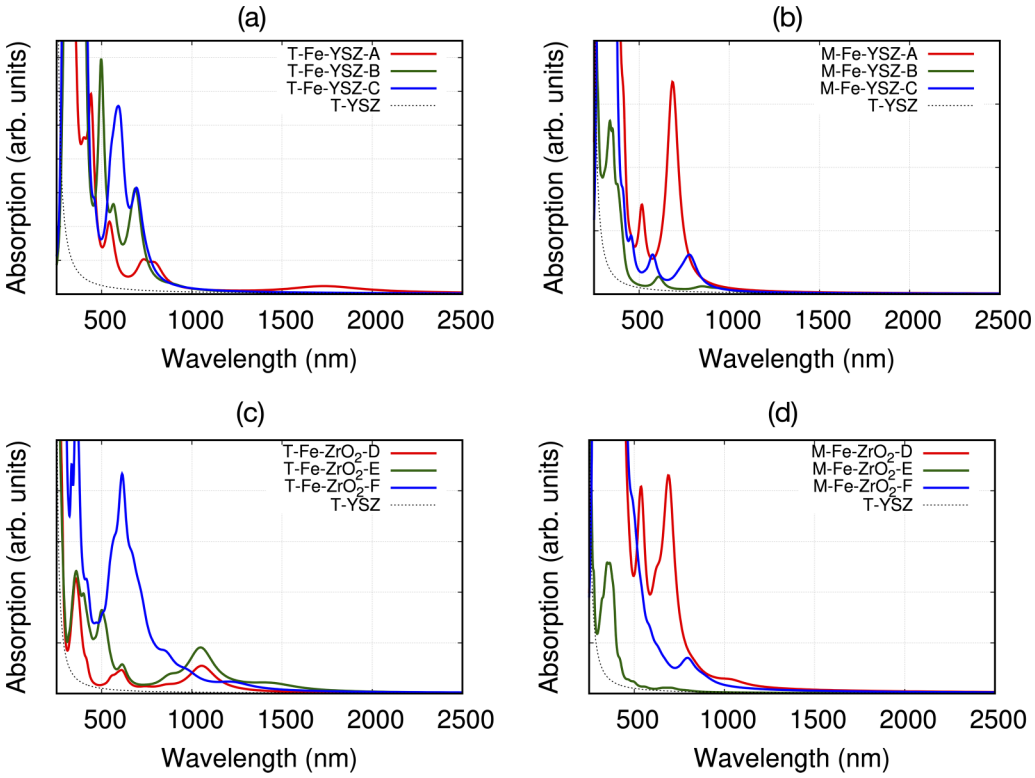

FIG. 8. G_0W_0-BSE calculated optical absorption spectra for the three configurations in (a) T-Fe-YSZ, (b) M-Fe-YSZ, (c) T-Fe-ZrO_2, and (d) T-Fe-ZrO_2. In each subfigure, the G_0W_0-BSE calculated T-YSZ optical spectrum (dotted black) is also given for reference.

multiple optical excitations are found between the 250 and 2000 nm wavelength range. Most of the prominent excitations (with relatively large absorption coefficients) exist between 400 and 700 nm, which corresponds to the wavelength in the visible light range of the electromagnetic spectrum. The optical E_gs extracted from the BSE Tauc plots indicate that these prominent bands are due to the excitations from the valence band to the conduction band.

1. Interpretation of measured Fe-ZrO_2 *optical absorption*

First, we focus on the relatively simpler Fe-ZrO_2 composition. Our G_0W_0-BSE calculated optical absorption spectra [Fig. 8(d)] shows an excitation at ∼1000 nm for the M-Fe-ZrO_2-D configuration. We also observe some background absorption for the M-Fe-ZrO_2-F configuration in the vicinity of the ∼1000 nm wavelength, whereas the local bond distortions in the M-Fe-ZrO_2-E configuration did not show any appreciable feature in the G_0W_0-BSE optical spectrum. One of the origins of the broad absorption band centered around 1000 nm is attributed to the local bond distortions in the M-Fe-ZrO_2-D configuration. It is also important to note that the excitations at ∼1000 nm for the M-Fe-ZrO_2-D configuration are present only in the G_0W_0-BSE optical spectrum and are absent in the G_0W_0-IPA optical spectrum [see Fig. S9(d)]. Our detailed excitonic analysis (Fig. 9) reveals that the excitation at this specific wavelength results from the Fe2-3*d* to Fe2-3*d* transition, with the assistance of Fe2-3*d* and O-2*p* orbital mixing. The binding energy (E_b) of this exciton is calculated as 2.14 eV using Eq. (3).

2. Interpretation of measured Fe-YSZ optical absorption

We now discuss the more complex Fe-YSZ composition. Among the independent crystal structures that we studied in this work, the local bond distortions in the T-Fe-ZrO_2 atomic configurations show prominent excitations in the 1000 nm wavelength range. All three configurations (T-Fe-ZrO_2-D, T-Fe-ZrO_2-E, and T-Fe-ZrO_2-F) contribute to the optical excitations [Fig. 8(c)] in the 1000 nm wavelength range. In addition, these structures also have relatively weak excitations in the 1200–1500 nm range. However, we are unable to

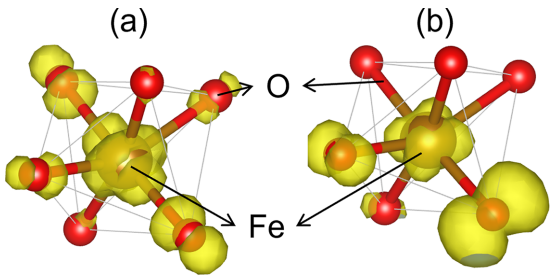

FIG. 9. Average electron and hole densities of the exciton correspond to the excitation at ∼1000 nm in M-Fe-ZrO_2-D atomic configuration. The yellow shaded area shows the average density of (a) electrons and (b) holes. The Fe cation corresponds to the Fe2 atom in Fig. 7(d). Since the Fe2-centered polyhedron contains most of the electron/hole distribution, we restrict the discussion of the excitonic effect in this local polyhedron. The binding energy (E_b) of this exciton is calculated as 2.14 eV. The relative strength of this exciton is highlighted in Fig. S13(a) in the Supplemental Material.

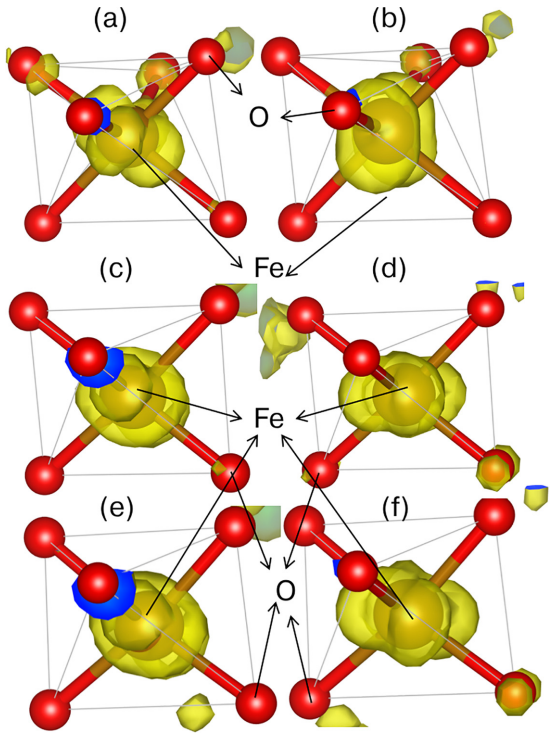

FIG. 10. Visualization in the real space of the charge density distributions for the first exciton between the 1000 and 1500 nm wavelength range in the T-Fe-ZrO_2-D (a) and (b), T-Fe-ZrO_2-E (c) and (d), and T-Fe-ZrO_2-F (e) and (f) atomic configurations. All excitons are localized at the Fe2-centered octahedron. The average electron density distributions are shown in (a), (c), and (e). The associated average hole electron density distributions are shown in (b), (d), and (f). The relative strengths of these excitons are highlighted in Figs. S13(b)–S13(d), respectively, in the Supplemental Material.

unambiguously identify these longer wavelength excitations in the experimentally measured optical absorption spectra, likely due to the strong contribution from the baseline absorption. It is also interesting to note that none of these excitations appear in the G_0W_0-IPA spectra, which is indicative of their excitonic origin, as shown in Figs. S8(d)–S8(f) in the Supplemental Material. In Fig. 10, we show the average electron and hole densities of the first exciton between 1000 and 1500 nm for the three T-Fe-ZrO_2 configurations. All excitations have a similar signature, i.e., being localized in the Fe2-3d orbitals with some O-2p mixing. However, their binding energies are different: 2.09 eV (T-Fe-ZrO_2-D), 1.96 eV (T-Fe-ZrO_2-E), and 1.49 eV (T-Fe-ZrO_2-F), which we attribute to the distinct local bond distortions in the Fe2-O polyhedra (Table II).

After T-Fe-ZrO_2, the next major contribution comes from the M-Fe-ZrO_2. Since the data was discussed in sufficient depth in Sec. III C 1, we focus on the next set of configurations that belong to the M-Fe-YSZ crystal structure. The G_0W_0-BSE optical absorption spectrum that represents the M-Fe-YSZ-B atomic configuration shows a weak excitation around 900 nm wavelength [Fig. 8(b)]. Its binding energy is calculated as 2.12 eV. The electron and hole densities for M-Fe-YSZ-B are shown in Fig. 11. Similar to the T-Fe-ZrO_2 structure, the excitons are localized in the Fe-3d orbitals with some O-2p mixing.

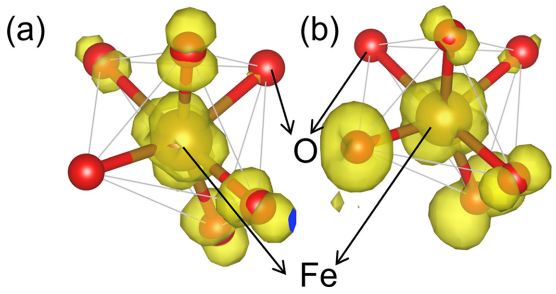

FIG. 11. Average electron (a) and hole (b) density distribution of the exciton corresponds to the excitation at ∼950 nm in M-Fe-YSZ-B. The relative strength of this exciton is highlighted in Fig. S13(e) in the Supplemental Material.

Finally, the G_0W_0-BSE calculated optical absorption spectra of the T-Fe-YSZ structure is shown in Fig. 8(a). No optical excitations are detected in the 1000 nm wavelength range. However, there is a weak excitation around the 1500–2000 nm wavelength range in the T-Fe-YSZ-A atomic configuration that is not present in the G_0W_0-IPA calculated optical absorption spectrum [Fig. S8(a) in the Supplemental Material]. This excitation corresponds to an exciton located at ∼1750 nm. The real space visualization of the average electron and hole densities of this exciton is shown in Figs. 12(a) and 12(b), respectively. Both electron and hole density distributions show two nodal planes on the Fe atom, which indicates that the electron and hole are located on the Fe-3d orbital. In addition, a relatively smaller population of electrons and holes is also found in the neighboring O atom, whose origin is likely due to the mixing of Fe-3d and O-2p orbitals. The presence of large baseline absorption in the experimental measured spectra (Fig. 4) makes it difficult to identify this excitation in the T-Fe-YSZ sample. Intriguingly, on increasing the Lorentzian broadening from 0.1 to 0.3 eV in our DFT-G_0W_0-BSE simulated spectra, we lose the broadband optical absorption around 1750 nm to the background [Fig. S12(c) in the Supplemental Material].

IV. SUMMARY

We synthesized two Fe-YSZ and Fe-ZrO_2 materials systems as a function of Fe concentration. Characterization based

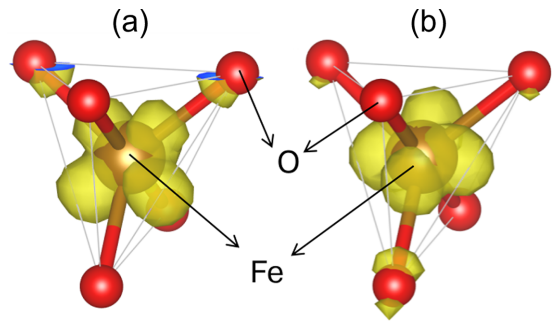

FIG. 12. Average electron and hole densities of the exciton at ∼1750 nm in Fig. 8(a) for the T-Fe-YSZ-A atomic configuration. The yellow shaded area shows the average density of (a) electrons and (b) holes. The relative strength of this exciton is highlighted in Fig. S13(f) in the Supplemental Material.

on XRD revealed important differences in the crystallographic phases formed consistent with the literature data. We also measured the optical absorption spectra of the materials in the UV-Vis-NIR wavelength range and observed a broad absorption band centered around the 1000 nm wavelength in both sets of material, albeit with subtle differences. There is, in addition, another broad absorption band centered around the 500 nm wavelength, which was previously reported [32]. The Kohn-Sham DFT was used to simulate 12 independent atomic configurations in two crystal structures (tetragonal and monoclinic) for two compositions (Fe-YSZ and Fe-ZrO_2). The local bond distortions in the tetragonal and monoclinic structures are found to be quite different. The tetragonal structures (in both Fe-YSZ and Fe-ZrO_2) were particularly found to be more sensitive to local bond distortions when compared to that of the monoclinic structures studied in this work. Given the known limitations of the Kohn-Sham DFT in predicting the excited state properties, we used the G_0W_0-BSE MBPT to calculate the optical absorption spectra. Our G_0W_0-BSE calculated optical absorption spectra are able to account for the optical excitations *likely* observed in the experimentally measured optical absorption of the Fe-YSZ and Fe-ZrO_2 samples. Our G_0W_0-BSE calculations predict that the local bond distortions in the three T-Fe-ZrO_2 atomic configurations (D, E, and F) have the relatively strongest excitations centered around the 1000 nm wavelength. Lack of experimental data (both from this work and in the literature) on the local structure information in Fe-YSZ precludes us from making definitive statements about the causal nature of these optical excitations. These suggest that high-resolution extended x-ray absorption fine-structure studies will be worthwhile. The excitonic effects due to the Fe-3d to Fe-3d electronic transitions (with some O-2p mixing) are predicted to be the origin for these ∼1000 nm wavelength optical excitations. Such Fe-3d to Fe-3d transitions are allowed in both Fe-YSZ and Fe-ZrO_2 systems because of the absence of the local inversion symmetry at the Fe sites caused by the bond distortions associated with the doping. The agreement between experimentally measured and MBPT simulated optical absorption spectra is an encouraging result because it establishes MBPT as a predictive approach to guide the compositional design of TBCs with tailored optical properties. We also recognize that the optical measurements are performed at 300 K, whereas the G_0W_0-BSE calculations are simulated at 0 K. The lack of incorporating electron-phonon and exciton-phonon interactions is a deficiency of the modeling effort discussed in this work. However, it has also been noted that one of the main effects of temperature on the BSE (in single-layer MoS_2) is the broadening of the spectral line shape and shifting of the excitons towards longer wavelengths (lower energies) [50]. As a result, our qualitative interpretation of the G_0W_0-BSE results, despite being performed at 0 K, are expected to also explain the origin of the optical measurements. The outcome of this work has key implications in the TBC composition region via band engineering to minimize the contribution of the radiative component of the total heat transfer.

ACKNOWLEDGMENTS

We gratefully acknowledge support from the Office of Naval Research Grants No. N00014-21-1-2478 and No. N00014-21-1-2479 managed by Dr. David Shifler. S.L. and P.V.B. thank the Rivanna high-performance computing cluster support staff at the University of Virginia for assistance with the compilation of the QUANTUM ESPRESSO and YAMBO codes. V.K.C. and D.R.C wish to thank Matthew Cabot for his assistance in the materials synthesis.

[1] R. A. Miller, Current status of thermal barrier coatings? An overview, Surf. Coat. Technol. **30**, 1 (1987).

[2] N. P. Padture, M. Gell, and E. H. Jordan, Thermal barrier coatings for gas-turbine engine applications, Science **296**, 280 (2002).

[3] D. R. Clarke and C. G. Levi, Materials design for the next generation thermal barrier coatings, Annu. Rev. Mater. Res. **33**, 383 (2003).

[4] U. Schulz, C. Leyens, K. Fritscher, M. Peters, B. Saruhan-Brings, O. Lavigne, J.-M. Dorvaux, M. Poulain, R. Mévrel, and M. Caliez, Some recent trends in research and technology of advanced thermal barrier coatings, Aerosp. Sci. Technol. **7**, 73 (2003).

[5] L. B. Chen, Yttria-stabilized zirconia thermal barrier coatings—A review, Surf. Rev. Lett. **13**, 535 (2006).

[6] R. Siegel and C. M. Spuckler, Approximate solution methods for spectral radiative transfer in high refractive index layers, Int. J. Heat Mass Transfer. **37**, 403 (1994).

[7] R. Siegel and C. M. Spuckler, Analysis of thermal radiation effects on temperatures in turbine engine thermal barrier coatings, Mater. Sci. Eng. A **245**, 150 (1998).

[8] I. O. Golosnoy, A. Cipitria, and T. W. Clyne, Heat transfer through plasma-sprayed thermal barrier coatings in gas turbines: A review of recent work, J. Therm. Spray Technol. **18**, 809 (2009).

[9] Q. Flamant and D. R. Clarke, Opportunities for minimizing radiative heat transfer in future thermal and environmental barrier coatings, Scr. Mater. **173**, 26 (2019).

[10] G. Lim and A. Kar, Radiative properties of thermal barrier coatings at high temperatures, J. Phys. D **42**, 155412 (2009).

[11] G. Koutsakis and D. R. Clarke, Optical absorption effects in thermal radiation barrier coating materials, Surf. Coat. Technol. **487**, 130974 (2024).

[12] D. L. Wood and K. Nassau, Refractive index of cubic zirconia stabilized with yttria, Appl. Opt. **21**, 2978 (1982).

[13] D. L. Wood, K. Nassau, and T. Y. Kometani, Refractive index of Y_2O_3 stabilized cubic zirconia: Variation with composition and wavelength, Appl. Opt. **29**, 2485 (1990).

[14] R. C. Buchanan and S. Pope, Optical and electrical properties of yttria stabilized zirconia (YSZ) crystals, J. Electrochem. Soc. **130**, 962 (1983).

[15] J.-H. Park and R. N. Blumenthal, High-temperature optical absorption measurement of single-crystal, yttria-stabilized zirconia, J. Am. Ceram. Soc. **71**, C462 (1988).

[16] T. Götsch, E. Bertel, A. Menzel, M. Stöger-Pollach, and S. Penner, Spectroscopic investigation of the electronic

structure of yttria-stabilized zirconia, Phys. Rev. Mater. **2**, 035801 (2018).

[17] J. A. Nychka, M. R. Winter, D. R. Clarke, T. Naganuma, and Y. Kagawa, Temperature-dependent optical reflectivity of tetragonal-prime yttria-stabilized zirconia, J. Am. Ceram. Soc. **89**, 908 (2006).

[18] J. I. Eldridge, C. M. Spuckler, and J. R. Markham, Determination of scattering and absorption coefficients for plasma-sprayed yttria-stabilized zirconia thermal barrier coatings at elevated temperatures, J. Am. Ceram. Soc. **92**, 2276 (2009).

[19] G. Stapper, M. Bernasconi, N. Nicoloso, and M. Parrinello, *Ab initio* study of structural and electronic properties of yttria-stabilized cubic zirconia, Phys. Rev. B **59**, 797 (1999).

[20] G. P. Cousland, X. Y. Cui, A. E. Smith, A. P. J. Stampfl, and C. M. Stampfl, Mechanical properties of zirconia, doped and undoped yttria-stabilized cubic zirconia from first-principles, J. Phys. Chem. Solids **122**, 51 (2018).

[21] M. Rohlfing and S. G. Louie, Electron-hole excitations and optical spectra from first principles, Phys. Rev. B **62**, 4927 (2000).

[22] J. Vinson, J. J. Rehr, J. J. Kas, and E. L. Shirley, Bethe-Salpeter equation calculations of core excitation spectra, Phys. Rev. B **83**, 115106 (2011).

[23] X. Leng, F. Jin, M. Wei, and Y. Ma, GW method and Bethe–Salpeter equation for calculating electronic excitations, WIREs Comput. Mol. Sci. **6**, 532 (2016).

[24] X. Blase, I. Duchemin, D. Jacquemin, and P.-F. Loos, The Bethe–Salpeter equation formalism: From physics to chemistry, J. Phys. Chem. Lett. **11**, 7371 (2020).

[25] S. M. Avdoshenko and A. Strachan, High-temperature emissivity of silica, zirconia and samaria from *ab initio* simulations: Role of defects and disorder, Modell. Simul. Mater. Sci. Eng. **22**, 075004 (2014).

[26] M. J. Verkerk, A. J. A. Winnubst, and A. J. Burggraaf, Effect of impurities on sintering and conductivity of yttria-stabilized zirconia, J. Mater. Sci. **17**, 3113 (1982).

[27] N. Matsui and M. Takigawa, Impedance spectroscopy on YSZ with iron oxide as additive, Solid State Ionics **40-41**, 926 (1990).

[28] Q. Dong, Z. H. Du, T. S. Zhang, J. Lu, X. C. Song, and J. Ma, Sintering and ionic conductivity of 8YSZ and CGO10 electrolytes with small addition of Fe_2O_3: A comparative study, Int. J. Hydrogen Energy **34**, 7903 (2009).

[29] F. Guo and P. Xiao, Effect of Fe_2O_3 doping on sintering of yttria-stabilized zirconia, J. Eur. Ceram. Soc. **32**, 4157 (2012).

[30] K. Chen, Y. Fan, Z. Hu, and Q. Yan, Study on the structure and reduction behaviour of the iron–zirconium oxide system, J. Mater. Chem. **6**, 1041 (1996).

[31] S. Davison, R. Kershaw, K. Dwight, and A. Wold, Preparation and characterization of cubic ZrO_2 stabilized by Fe(III) and Fe(II), J. Solid State Chem. **73**, 47 (1988).

[32] H. Nakajima, K. Itoh, H. Kaneko, and Y. Tamaura, Effects of Fe doping on crystalline and optical properties of yttria-stabilized zirconia, J. Phys. Chem. Solids **68**, 1946 (2007).

[33] J. Zhao, Z. Shen, W. Si, and X. Wang, Bi-colored zirconia as dental restoration ceramics, Ceram. Int. **39**, 9277 (2013).

[34] J. Chen, Y. Zhang, S. Dong, L. Zhao, B. Gu, N. Liao, and N. Wen, Effect of coloration with various metal oxides on zirconia, Coloration Technol. **131**, 27 (2015).

[35] F. Tabatabaian, Color aspect of monolithic zirconia restorations: A review of the literature, J. Prosthodontics **28**, 276 (2019).

[36] F. J. Berry, M. H. Loretto, and M. R. Smith, Iron-zirconium oxides: An investigation of structural transformations by x-ray diffraction, electron diffraction, and iron-57 Mössbauer spectroscopy, J. Solid State Chem. **83**, 91 (1989).

[37] F. Guo, X. Zhang, H. Cai, X. Fan, L. Hu, W. Sun, and X. Zhao, Effect of doping location induced anisotropy on thermophysical properties of dilute Fe_2O_3-Y_2O_3-ZrO_2 solid solutions, J. Am. Ceram. Soc. **104**, 4742 (2021).

[38] P. Li, I.-W. Chen, and J. E. Penner-Hahn, Effect of dopants on zirconia stabilization? An x-ray absorption study: I, trivalent dopants, J. Am. Ceram. Soc. **77**, 118 (1994).

[39] A. G. Belous, E. V. Pashkova, K. V. Kravchyk, V. P. Ivanitskii, and O. I. V'yunov, Mössbauer and x-ray diffraction studies of cubic solid solutions of the ZrO_2–Y_2O_3–Fe_2O_3 system, J. Phys. Chem. C **112**, 3914 (2008).

[40] J.-P. Jolivet, M. Henry, and J. Livage, *Metal Oxide Chemistry and Synthesis: From Solution to Solid State* (Wiley, New York, 2000).

[41] V. K. Champagne III, G. Pisaturo, and D. R. Clarke, High temperature oxides for selective absorption of thermal radiation, J. Eur. Ceram. Soc. **43**, 7656 (2023).

[42] P. Giannozzi, S. Baroni, N. Bonini, M. Calandra, R. Car, C. Cavazzoni, D. Ceresoli, G. L. Chiarotti, M. Cococcioni, I. Dabo *et al.*, QUANTUM ESPRESSO: A modular and open-source software project for quantum simulations of materials, J. Phys.: Condens. Matter **21**, 395502 (2009).

[43] P. Giannozzi, O. Andreussi, T. Brumme, O. Bunau, M. Buongiorno Nardelli, M. Calandra, R. Car, C. Cavazzoni, D. Ceresoli, M. Cococcioni *et al.*, Advanced capabilities for materials modelling with QUANTUM ESPRESSO, J. Phys.: Condens. Matter **29**, 465901 (2017).

[44] J. P. Perdew, K. Burke, and M. Ernzerhof, Generalized gradient approximation made simple, Phys. Rev. Lett. **77**, 3865 (1996).

[45] M. Schlipf and F. Gygi, Optimization algorithm for the generation of ONCV pseudopotentials, Comput. Phys. Commun. **196**, 36 (2015).

[46] H. J. Monkhorst and J. D. Pack, Special points for Brillouin-zone integrations, Phys. Rev. B **13**, 5188 (1976).

[47] D. K. Smith and W. Newkirk, The crystal structure of baddeleyite (monoclinic ZrO_2) and its relation to the polymorphism of ZrO_2, Acta Crystallogr. **18**, 983 (1965).

[48] See Supplemental Material at http://link.aps.org/supplemental/10.1103/PhysRevMaterials.8.085203 for the data on DFT relaxed crystal structures for all 12 configurations, experimentally measured densities of the sintered materials, G_0W_0 convergence testing, fundamental band gaps from Kohn-Sham DFT and G_0W_0 quasiparticle corrections, real and imaginary parts of the dielectric functions from both G_0W_0-BSE and G_0W_0-IPA approximations, optical absorption spectra from both G_0W_0-BSE and G_0W_0-IPA approximations, refractive index and extinction coefficients from both G_0W_0-BSE and G_0W_0-IPA approximations, and impact of Lorentzian broadening on the G_0W_0-BSE calculated optical absorption spectra.

[49] A. Marini, C. Hogan, M. Grüning, and D. Varsano, YAMBO: An ab initio tool for excited state calculations, Comput. Phys. Commun. **180**, 1392 (2009).

[50] D. Sangalli, A. Ferretti, H. Miranda, C. Attaccalite, I. Marri, E. Cannuccia, P. Melo, M. Marsili, F. Paleari, A. Marrazzo

et al., Many-body perturbation theory calculations using the YAMBO code, J. Phys.: Condens. Matter **31**, 325902 (2019).

[51] F. Bruneval and X. Gonze, Accurate *GW* self-energies in a plane-wave basis using only a few empty states: Towards large systems, Phys. Rev. B **78**, 085125 (2008).

[52] Z. Qiu, M. Trushin, H. Fang, I. Verzhbitskiy, S. Gao, E. Laksono, M. Yang, P. Lyu, J. Li, J. Su, M. Telychko, K. Watanabe, T. Taniguchi, J. Wu, A. H. C. Neto, L. Yang, G. Eda, S. Adam, and J. Lu, Giant gate-tunable bandgap renormalization and excitonic effects in a 2D semiconductor, Sci. Adv. **5**, eaaw2347 (2019).

[53] A. J. Jackson, A. M. Ganose, A. Regoutz, R. G. Egdell, and O. D. Scanlon, GALORE: Broadening and weighting for simulation of photoelectron spectroscopy, J. Open Source Software **3**, 773 (2018).

[54] S. V. Bechta, E. V. Krushinov, V. I. Almjashev, S. A. Vitol, L. P. Mezentseva, Y. B. Petrov, D. B. Lopukh, V. B. Khabensky, M. Barrachin, S. Hellmann *et al.*, Phase diagram of the ZrO_2–FeO system, J. Nucl. Mater. **348**, 114 (2006).